

Negative ion characterization in a helicon plasma source for fusion neutral beams by Cavity Ring-Down Spectroscopy and Langmuir Probe laser photodetachment

R Agnello¹, S Béchu², I Furno¹, Ph Guittienne³, A A Howling¹, R Jacquier¹, G Plyushchev¹, M Barbisan^{4,5}, R Pasqualotto⁴, I Morgal⁶, A Simonin⁶

¹Ecole Polytechnique Fédérale de Lausanne (EPFL), Swiss Plasma Center (SPC), CH-1015 Lausanne, Switzerland

²Université Grenoble-Alpes, CNRS, Grenoble INP, LPSC-INP23, 38000 Grenoble, France

³Helyssen, Route de la Louche 31, CH-1092 Belmont-sur-Lausanne, Switzerland

⁴Consorzio RFX, Corso Stati Uniti 4, I-35127 Padova, Italy

⁵INFN-LNL, Viale dell'Università 2, I-35020 Legnaro, Italy

⁶CEA, IRFM, F-13108 St-Paul-lez-Durance, France

E-mail: riccardo.agnello@epfl.ch

Abstract.

Negative ions are characterized in the helicon plasma source RAID (Resonant Antenna Ion Device) at the Swiss Plasma Center by means of Cavity Ring-Down Spectroscopy (CRDS) and Langmuir Probe (LP)-assisted laser photodetachment. A high density and axially homogeneous plasma column is produced via a RF antenna able to sustain the propagation of helicon waves in a steady state regime. An electron density $n_e \cong 2.0 \times 10^{18} \text{ m}^{-3}$ in H_2 plasma at 0.3 Pa and 3 kW of input power is measured in the center of the plasma column by LP and microwave interferometry. The electron temperature profile is peaked on axis reaching $T_e \approx 5 \text{ eV}$ and decreasing to 1.5 eV at $r = 0.05 \text{ m}$. Thus, a hot core region forms where H_2 molecules are rovibrationally excited ($\text{H}_2(\nu)$), and a cold edge, where low energy electrons can attach to $\text{H}_2(\nu)$ and produce H^- ions by dissociative attachment. In this work we use LP-assisted laser photodetachment and CRDS diagnostics to measure H^- and D^- radial density profiles and how they depend on source parameters. We show that negative ions are distributed on a shell of 0.06 m radius with a peak value of $\sim 2.0 \times 10^{16} \text{ m}^{-3}$ in H_2 plasma. These results suggest that, although substantial technical development is needed, helicon plasmas could be considered as a possible candidate as sources of negative ions for future NBIs.

1. Introduction

Negative ion based Neutral Beam Injectors (NBIs) for fusion applications require high accelerated negative ion currents, and current density, with the ion energy of the order of 1 MeV. In conventional NBI systems, positive ions, usually H^+ or D^+ , are accelerated by electric fields and neutralized by charge exchange with gas molecules. The neutralization efficiency, however, drops to negligible values for energies greater than 250 keV, rendering gas neutralization impracticable for positive ions [1]. The neutralization efficiency of negative H^- or D^- ions in gas neutralizers, is around 60% at the energy requirements of NBIs, rendering negative ions much more attractive. For example, ITER's negative ion-based NBI will deliver 16.7 MW of D^0 at 1 MeV [2]. The negative ions for ITER will be produced by Inductively-Coupled Plasma (ICP) sources requiring several hundreds of kW of RF power and the evaporation of caesium to enhance the negative ion production by surface processes [3]. For the next generation of NBI fusion devices, less power consumption will be essential to increase the overall efficiency of the power plant. This is crucial considering that DEMO NBI design will be driven by Reliability, Availability, Maintainability, Inspectability (RAMI) and high efficiency requirements [4]. In this context, helicon plasma sources could be considered to serve as sources of negative ions for NBIs for a number of reasons. First, helicon plasma sources require less RF power compared to ICP sources to reach similar plasma density parameters [5]. Second, they can operate more easily than ICPs at pressures < 0.3 Pa, which is essential in order to reduce to acceptable levels the negative ion losses due to electron stripping in the extractor and accelerator in a future NBI system. Third, negative ions are efficiently produced in volume [6], although it remains to be demonstrated that the yield is sufficiently high to avoid the use of Cs. Although helicon plasma sources have been extensively studied for their potential application for space thrusters [7], their application in fusion remains largely unexplored to date.

The implementation of a helicon-based negative ion source requires the investigation of negative ion physics including both experimental and theoretical efforts, as well as ensuring that the source will be compatible with an extractor and an acceleration system. Research performed in the Resonant Antenna Ion Device (RAID) [8] at the Swiss Plasma Center aims at broadening the current knowledge of the physics of volume production of negative hydrogen and deuterium ions in helicon plasmas, which has been explored, apart from RAID, to the best of our knowledge, only in a few helicon plasma devices [9, 10]. The possible integration of such a source, if able to reach the RAMI and efficiency requirements compatible for future NBIs, requires considerable experimental, numerical and technical development. At this early stage of development, one relevant physics goal, which can be addressed on RAID, is to understand how the volume negative ion production yield depends on helicon plasma parameters such as the RF power, the neutral pressure and the magnetic field geometry.

RAID can sustain steady state plasma discharges in different gases, including H_2 , D_2 , using a resonant antenna in a birdcage geometry [11]. In RAID, many

76 basic plasma diagnostics including Langmuir Probes (LPs), microwave interferometry,
77 magnetic probes, Optical Emission Spectroscopy (OES) and diagnostics based on
78 laser-plasma interaction, such as LP-assisted laser photodetachment and Cavity Ring-
79 Down Spectroscopy (CRDS), are routinely employed [12, 13]. Previous experimental
80 campaigns based on OES and CRDS revealed a significant amount of negative ions both
81 in hydrogen and deuterium plasmas [6, 14]. Both OES and CRDS measure negative ion
82 density in the order of a few 10^{16} m^{-3} , and development is needed to reach the negative
83 ion densities required for NBIs, which is 10^{17} m^{-3} [15]. The main advantage of CRDS
84 is that it allows a direct measurement of the absolute value of the negative ion density
85 without requiring any calibration and being non-invasive. However, the line-integrated
86 measurement does not provide the local density. In a previous experimental campaign,
87 we tested the robustness of CRDS and studied the experimental challenge of how to
88 reduce undesired effects that could deteriorate the accuracy of the measurement [14]. In
89 this paper, we extensively exploit CRDS by varying plasma parameters in combination
90 with LP-assisted laser photodetachment to deduce absolute negative ion density local
91 profiles. The knowledge of these profiles is important since they are used as input
92 parameters for negative ion extraction and modeling.

93 The paper is organized as follows: Section 2 describes the plasma source RAID.
94 In Section 3, we present the experimental setup of CRDS and LP-assisted laser
95 photodetachment on the RAID device. Section 4 shows the experimental results in
96 H_2 and D_2 by varying the plasma parameters, and Section 5 discusses the conclusions
97 and future perspectives.

98 2. The Resonant Antenna Ion Device (RAID)

99 RAID, shown in Fig. 1, produces a magnetized plasma column by means of a resonant
100 antenna in a birdcage geometry [8]. The cylindrical vacuum vessel is surrounded by six
101 coils producing an axial magnetic field up to 800 G on axis. The first coil on the left is
102 usually operated in inverse polarity with respect to the other five to create a gradient of
103 magnetic field along the axis in the antenna region. This enhances the electron confine-
104 ment in the antenna probably because slower electrons produced in the antenna region
105 are confined by the bottleneck of the magnetic field. This was experimentally seen to
106 facilitate the ignition of the plasma discharge and to stabilize the helicon regime. A va-
107 riety of axial boundary conditions can be implemented. In the present experiments, the
108 plasma column is bounded behind the antenna by a ceramic foam, and on the far end
109 by a water-cooled grounded copper end-plate. A stable helicon regime can be attained
110 with a minimum power of 1000 W for hydrogen and deuterium. A traveling helicon
111 wave has been measured by means of a magnetic probe [13] confirming that the plasma
112 column is sustained by helicon waves.

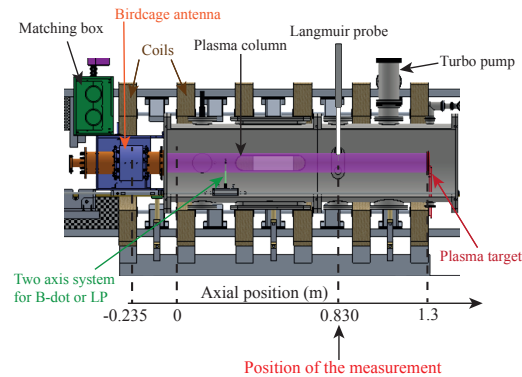


Figure 1. A cross section of the RAID plasma device along the axis. The cylindrical vacuum vessel of 1.4 m length and 0.4 m diameter is surrounded by six coils producing an axial magnetic field up to 800 G. The resonant birdcage antenna, placed on the left, produces a plasma column up to the target on the right.

114 2.1. Electron density and temperature profiles

115 Electron density and temperature along the vessel are measured by means of a movable
 116 LP on a two-axis system. Electrons are magnetized, with a Larmor radius which is
 117 comparable to, or even smaller than, the LP radius, making the analysis of IV curves
 118 to extract the absolute value of n_e unreliable. Ions, however, are not magnetized. We
 119 estimate ~ 0.1 eV for the ion temperature by assuming approximate thermal equilibrium
 120 with the neutral gas whose temperature ~ 1000 K is obtained from spectroscopic
 121 measurements [6]. In a magnetic field of 200 G, this gives an ion Larmor radius
 122 of ~ 1.6 mm, much bigger than the LP tip radius (0.2 mm). Absolute electron
 123 density profiles are therefore obtained with a LP in combination with a 100 GHz
 124 microwave heterodyne interferometer or by Thomson Scattering diagnostic, currently in
 125 the commissioning phase. In the rest of the manuscript, we will refer to "fill pressure"
 126 for the gas pressure measured in the vacuum vessel prior to operation of the helicon
 127 device. In hydrogen, a typical peak electron density of $2.0 \times 10^{18} \text{ m}^{-3}$ with 3 kW of
 128 injected power at 0.3 Pa fill pressure is usually achieved as depicted in Fig. 2, showing
 129 the electron density measured along the plasma vessel. The origin of the radial profile
 130 corresponds to the axis of the vacuum vessel.

131 The electron density along the axis of the plasma is quite uniform ($\pm 5\%$) in the region
 132 downstream of the antenna in the axial position between 0.4 m to 1.1 m.

133 Fig. 3(a) shows the electron density radial profile, measured at the axial position
 134 0.830 m, which strongly increases with RF power, as expected by power balance
 135 considerations [16]. The helicon wave power is deposited along the plasma column
 136 and, in steady state equilibrium, results in radially peaked n_e profiles. The T_e profiles
 137 shown in Fig. 3(b) are, however, only weakly dependent on the RF power. This can
 138 be explained with simple particle balance considerations: at this plasma regime, the
 139 electron temperature is independent of the plasma density and therefore the input power,

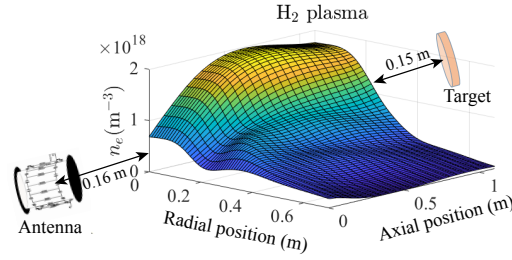


Figure 2. 3D cylindrically-symmetric interpolated profile of plasma density in the vessel measured with a two axis LP and calibrated with a 100 GHz heterodyne microwave interferometer. Measurements start 0.16 m from the near end of the antenna and stop 0.15 m before the target.

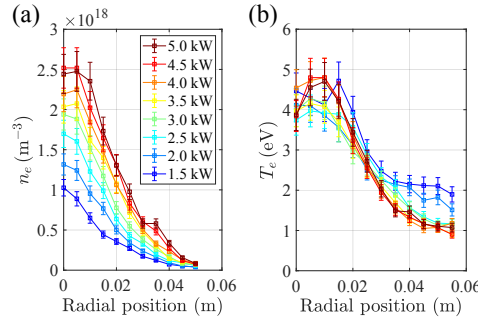
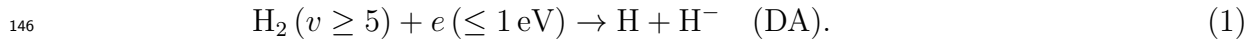
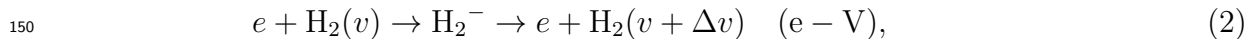


Figure 3. (a) Radial electron density and (b) temperature profile for a H_2 plasma at 0.3 Pa fill pressure and 200 G magnetic field on axis for different RF powers, at the axial position 0.830 m. The density profile n_e is obtained from LP measurements calibrated with interferometry. The T_e profiles are weakly dependent on the RF power.

140 depending only on the gas pressure [16]. Similar behaviours are observed in other helicon
 141 sources [17]. The n_e and T_e profiles are measured with a L-shaped Langmuir probe (0.2
 142 mm diameter and 10 mm long) located at axial position 0.830 m and vertically movable.
 143 The peaked T_e profile is favorable for the volume production of H^- since it provides a
 144 central hot region to rovibrationally excite the H_2 molecules and a cold external region
 145 where low energy electrons can produce the H^- by dissociative attachment (DA) [18, 19]:

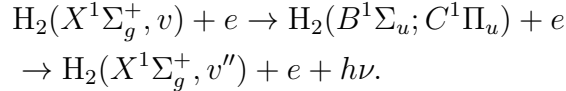


147 There are two possible mechanisms to produce the rovibrationally excited $\text{H}_2(v)$ in
 148 volume. The first is the stepwise vibrational excitation of molecules in collision with
 149 electrons (e-V process):



151 this reaction, however, requires many collisions to increase the vibrational state to high
 152 values since the most probable change in v is $\Delta v = \pm 1$ [20]: At the low pressure typical

153 of ions sources for NBIs, another important contribution to the production of the excited
 154 $\text{H}_2(v)$ is the radiative decay from singlet state, the so called E-V process [21]:



155 Previous experiments based on Optical Emission Spectroscopy (OES) and CRDS
 156 revealed a significant volume production of H^- and D^- [6]. The radial distribution
 157 measured by OES suggests that negative ions reach a maximum density in a radial shell
 158 located around $r \sim 4$ cm. Since CRDS was demonstrated to be a robust diagnostic, it is
 159 used here for an experimental campaign to broaden knowledge of negative ion physics
 160 in the present experimental device and to form a database for models of negative ion
 161 production in the helicon plasma. In order to make measurements comparable with
 162 the previous campaign [14], the same experimental setup was used as described in 3,
 163 combined with a movable LP to measure the radial profile of negative ion density using
 164 laser photodetachment.

165 3. Experimental setup: laser-based diagnostics for negative ions

166 To obtain absolute H^- and D^- radial density profiles, the measurements of CRDS and
 167 LP-assisted laser photodetachment were combined. CRDS has a fixed measurement
 168 position and is used to calibrate the relative radial profiles obtained by the LP-assisted
 169 laser photodetachment. The optical setups for the CRDS and for the LP-assisted
 170 photodetachment are respectively shown in Fig. 4(a) and in Fig. 4(b). In Fig. 4(a),
 171 the measurement position of the laser is fixed at $r = 0.04$ m (where we expect the
 172 largest density of H^- according to OES measurements [6]) and the laser beam performs
 173 multiple reflections between the two high reflectivity (HR) mirrors.

174 The CRDS technique was developed in 1988 by A. O'Keefe [22] to perform optical
 175 absorption measurements. CRDS is nowadays routinely used in fusion research as a
 176 plasma diagnostic to measure H^- and D^- line densities in negative ion sources [15, 23].
 177 To detect these ions, a pulsed Nd:YAG laser is employed [24]. The photon energy
 178 ($E = 1.2$ eV, corresponding to a wavelength of $\lambda = 1064$ nm) is sufficient to strip the
 179 weakly bound electron of H^- and D^- ($E_{\text{binding}} = 0.75$ eV) by photodetachment:



181 The CRDS diagnostic on RAID relies on an optical cavity made of two HR mirrors
 182 ($R > 99.998\%$ [24]) to multiply the interaction length with the absorbing medium.
 183 The light stored in the cavity is lost with an exponential decay time τ depending on
 184 the mirrors' reflectivity and the medium's absorption. Further details on the CRDS
 185 diagnostic in RAID can be found in Ref. [14]. An example of a CRDS signal in RAID
 186 is shown in the inset in Fig. 5. The line-integrated negative ion density \bar{n}_- is:

$$187 \quad \bar{n}_- = \int n_-(l) dl, \quad (4)$$

188 where n_- is the local negative ion density. The line-averaged negative ion density $\langle n_- \rangle$
 189 is given by:

$$190 \quad \langle n_- \rangle = \frac{1}{\sigma_-} \frac{L}{cd} \left(\frac{1}{\tau} - \frac{1}{\tau_0} \right), \quad (5)$$

191 where τ and τ_0 are the decay times in the presence and absence of absorbing medium
 192 (H^- or D^-). L is the cavity length, σ_- the photodetachment cross section, c the speed
 193 of light and d the distance over which the density is averaged. Thus, the line-integrated
 negative ion density is $\bar{n}_- = d \cdot \langle n_- \rangle$. The reflectivity of the mirrors is a key parameter

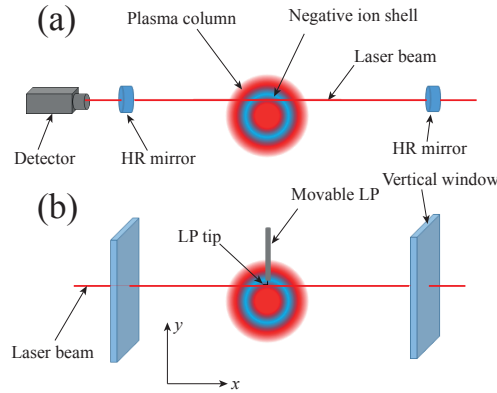


Figure 4. A schematic of the two different experimental setups employed: in (a) the CRDS and, in (b) the LP-laser photodetachment scheme. In (a) the measurements position of the laser is fixed at 4 cm. In (b) the laser beam is vertically displaced simultaneously with the LP.

194 since it determines the signal-to-noise ratio and hence the minimum detectable negative
 195 ion density.
 196

197 CRDS at a fixed measurement position is not sufficient to determine the local negative
 198 ion density since the CRDS signal is determined by the interaction between the photons
 199 in the laser beam and the plasma all along the path of the laser beam in the plasma.
 200 Moving the laser beam across the plasma column would allow to Abel invert the data
 201 to reconstruct the n_- radial profile. However, this method is impracticable due to
 202 the lengthy alignment procedure. LP-assisted laser photodetachment can be used
 203 to obtain relative negative ion profiles with a spatial precision comparable to the
 204 laser beam diameter. The movable LP employed on RAID for the LP-assisted laser
 205 photodetachment is shown schematically in Fig. 4(b). The laser measurement position
 206 can be varied simultaneously with the movable LP, which can be vertically displaced.
 207 The probe is displaced by a stepper motor and the vacuum is maintained by a bellows.
 208 The probe tip is aligned co-axially with the direction of the laser beam and biased
 209 at $V_{\text{bias}} = 26 \text{ V}$, above the plasma potential V_{plasma} , which is $V_{\text{plasma}} = 12(\pm 1) \text{ V}$ for
 210 $r < 0.06 \text{ m}$, for both H_2 and D_2 plasmas, and independent of gas pressure. The H^- or
 211 D^- ions in the laser path are photoneutralized and the stripped electrons are collected
 212 by the probe. This causes a sudden increase of the signal detected by the LP, in the

order of a fraction of microsecond, proportional to the local negative ion density. An example of a photodetachment signal in RAID is shown in Fig. 7. The fast transient is measured by a current probe consisting of a toroidal current transformer. The local negative ion density n_- can be estimated as follows:

$$\frac{n_-}{n_e} = \frac{I_{pd}}{I_{dc}}, \quad (6)$$

where n_e is the local electron density, I_{dc} the collected current at the V_{bias} , and I_{pd} the amplitude of the variation of the collected current due to the photodetachment. Eq. (6) can be applied if the following criteria are satisfied [25]: 1) the laser wavelength is suitable to photo-detach the electrons of the negative ions (i.e. the photon energy and the detachment cross section are sufficiently high), 2) the laser pulse energy is enough to photodetach all negative ions in the target volume, 3) the laser beam must have a minimum diameter from which the amplitude of the signal does not increase with beam diameter and, 4) the probe bias must be above the plasma potential. These criteria are satisfied as described above and in section 4.2.

4. Experimental Results

The CRDS and the LP-assisted photodetachment were used in two distinct experimental campaigns in H_2 and D_2 plasmas with 200 G magnetic field on the axis of RAID, and variable gas pressures.

4.1. CRDS characterization in RF power and gas pressure at a fixed Line-Of-Sight (LOS)

CRDS measurements are performed employing the technique described below, which was already introduced in [14] and reviewed here for clarity. Fig. 5 shows τ , the ring-down time, as a function of time, before, during, and after a H_2 plasma discharge with 5 kW RF power. The laser is pulsed at 10 Hz so that the temporal resolution is of the order of 0.1 s. The plasma discharge starts at $t \cong 30$ s in the presence of a mixture of H_2 and Ar gas (see Fig. 5); the Ar gas is added to facilitate plasma ignition [14]. The drop of τ just after plasma ignition is due to a combination of the absorption of the laser pulse by negative ions and the thermal stress of the optical cavity. Just after plasma ignition, Ar is removed in a few seconds and RF power is increased meanwhile. In the plateau where $\tau \cong 37 \mu\text{s}$, the plasma consists purely of H_2 and it is steady state. The plasma discharge is then turned off at $t \cong 80$ s causing the sudden increase of τ . To determine the line-integrated negative ion density \bar{n}_- , τ is linearly fitted 10 s before and after the τ sudden increase, so that accurate values of τ just before and after the jump can be estimated. The τ after the plasma shut down does not recover immediately to the pre-discharge value since the optical cavity was deformed by thermal stress during the plasma discharge. After a few tens of seconds, the complete recovery to the pre-discharge value is observed.

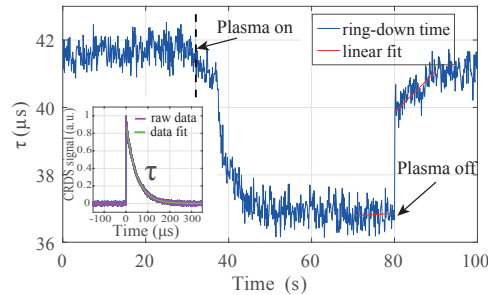


Figure 5. Ring-down time τ before, during, and after a plasma discharge for a H_2 plasma and 5 kW RF power. The plasma discharge starts at $t \cong 30$ s and it is stabilized after a few seconds. Plasma is turned off at $t = 80$ s causing the jump of τ due to the disappearance of H^- ions. The linear fit of tau before and after the plasma off is used to accurately determine τ at plasma off. The jump is used to evaluate the line-averaged H^- density. The inset shows a fit as used to calculate the ring-down time for each data point τ .

250 Thus, the accuracy of the measurement relies on the determination of the τ jump,
 251 whose detectability in turn depends on the mirrors' reflectivity and optical cavity's
 252 stability. Once the reliability of the technique was established [14], power scans were
 253 performed. Fig. 6 shows measurements with H_2 and D_2 plasma for different RF powers
 254 and gas pressures. H^- and D^- line-integrated density increase with RF power for both
 255 plasmas. For power larger than 4 kW, however, the growth rate is reduced for H^- . Note
 256 that these values are obtained in CW operation on RAID, so the production of negative
 257 ions is in a stationary regime. The data in H_2 are up to 8 kW of power and four gas
 258 pressures: 0.2 Pa, 0.3 Pa, 0.4 Pa and 0.5 Pa, the data in D^- are shown up to 5 kW at
 259 0.3 Pa because at the time of the experiments the impedance matching system was not
 260 calibrated for powers larger than 5 kW and we were mostly interested in the pressure
 261 relevant for application for NBI, namely 0.3 Pa. We remark that RAID operation
 262 at 0.2 Pa is possible, but results in a reduced performance. For these experimental
 263 investigations we chose to operate at 0.3 Pa as a compromise between a good signal-
 264 to-noise ratio and the low pressure requirements for the NBI applications. The line-
 265 integrated negative ion density appears to increase with fill pressure, but this is not
 266 helpful, given the low pressure requirements for NBI applications.

267 4.2. LP-assisted laser photodetachment to determine radial n_- profiles

268 LP-assisted photodetachment has the main advantage of providing information on the
 269 local value of negative ion density according to eq. 5, although it is more perturbing
 270 than CRDS. In Fig. 7, typical photodetachment signals in a H_2 plasma for increasing
 271 RF powers are shown. Photodetachment signals are averaged over 200 laser pulses. To
 272 filter out the DC component of the signal collected when the probe bias is at V_{bias} from
 273 the fast transient due to the photodetachment, an AC decoupling circuit, consisting of

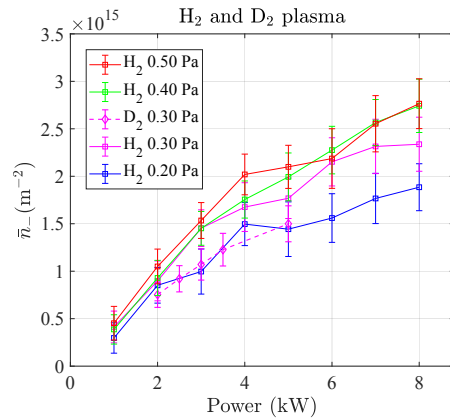


Figure 6. Line-integrated negative ion density as a function of RF power at different pressures for H_2 and D_2 plasmas, demonstrating the steady-state production of negative ions up to 8 kW of RF power.

274 a high pass filter, was initially used. However, in order to avoid the distortion of the
 275 signal due to the bandwidth of the circuit, we finally employed an AC toroidal current
 276 transformer (FTC-016, 10:1) with 2.5 V/A sensitivity and upper cut-off frequency at
 277 1.17 GHz. In Fig. 7, the laser pulse strikes the LP tip at $t = 0$ s causing the overshoot
 278 (increase of the collected electron current) whose amplitude is indicated by the vertical
 279 arrow for the 5 kW case. The subsequent undershoot and the lack of "plateau" has
 280 been reported by other authors such as by P. Devynck et al. [26], M. Bacal [25] and
 281 S. Aleiferis [27]. This effect is partly due to the motion of ions caused by the thermal
 282 motion of the electrons [28]. The large undershoot and the double peak might also be
 283 an effect of the magnetized electrons. Ions are however not magnetized for the magnetic
 284 fields employed for these tests (200G). Numerical simulations using a particle-in-cell
 285 code are presently under way to fully model the temporal dynamics of the observed
 286 photodetachment signal. If the laser pulse strikes the probe when there is no plasma, no
 287 variation of the signal is detected. The amplitude increases with RF power confirming
 288 the trend observed during CRDS tests.

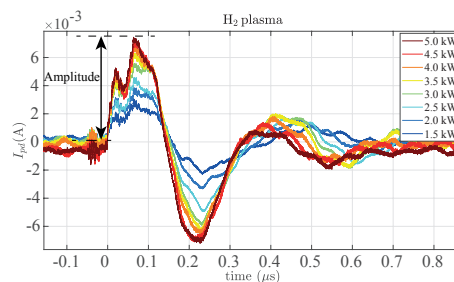


Figure 7. Typical photodetachment signals for a H_2 plasma. The laser strikes the LP tip at $t = 0$ s causing the overshoot whose amplitude is indicated by the arrow.

290 H^- to satisfy (6). This was performed by increasing the laser pulse energy and observing
 291 the I_{pd} saturation from a pulse energy of 35 mJ. Consequently, all results were obtained
 292 using a pulse energy of 50 mJ.

293 To radially characterize the plasma, the LP is moved in the vertical direction. For
 294 each position, a new alignment laser beam-probe is needed. Fig. 8 summarizes the
 295 results obtained with laser photodetachment while varying the RF power. The left and
 296 the right column show the results for H_2 and D_2 plasmas respectively. The gas filling
 297 pressure was 0.3 Pa.

298 In Fig. 8(a) the amplitudes of the photodetachment signals are shown. On average, a
 299 weaker signal is measured in the case of D_2 . As suggested by Eq. (6), the shape of the
 300 curve is due to a combination of the negative ion density and the electron temperature.
 301 Fig. 8(b) shows the electron current I_{dc} when the probe is biased at $V_{\text{bias}} = 26 \text{ V}$,
 302 above the plasma potential. On average, more electrons are collected in the case of
 303 D_2 suggesting that the electron density is higher in this plasma. It was not possible to
 304 perform measurements for $r < 0.04 \text{ m}$ because I_{dc} was too high and risked damaging the
 305 system. Moreover, the window height limited the LOS of the laser to $r < 0.065 \text{ m}$.

306 Fig. 8(c) shows the ratios n_{H^-}/n_e and n_{D^-}/n_e , given by Eq. (6). Although the electrons
 307 are magnetized, the electron transport coefficient is the same both for the photodetached
 308 electrons and for the electrons collected by the probe when biased above V_{plasma} .
 309 Therefore, the transport coefficients tend to cancel out in the ratio. We note the strong
 310 difference between the two plasmas. At $r = 0.06 \text{ m}$, n_{H^-}/n_e reaches 0.3, while n_{D^-}/n_e
 311 reaches about 0.05. The ratio n_{H^-}/n_e is comparable to the value obtained in ICP sources,
 312 with moderate source conditioning, close to the extraction grid, at 0.4 Pa pressure and
 313 55 kW power, using the same technique [29]. However, a comparable n_{H^-}/n_e does not
 314 necessarily imply that the extracted negative ion current from a hypothetical helicon
 315 source will be comparable to ICP. The magnetic field employed for these experiments
 316 (200G) is double compared to the magnetic filter field of ICP sources leading to different
 317 transport of the relevant species.

318 Also, the profile ratios are only weakly dependent on power, as shown in Fig. 8(c). The
 319 independence of the ratio n_-/n_e might be an advantage because it makes the negative
 320 ion yield in the source easier to tune. The reason of this difference between n_{H^-}/n_e and
 321 n_{D^-}/n_e is mainly due to the higher electron density measured in D_2 plasma, as shown in
 322 Fig. 8(d). At 5 kW power and $r = 0.04 \text{ m}$ (where the fixed LOS of CRDS is located) n_e
 323 attains $1.3 \times 10^{17} \text{ m}^{-3}$ in H_2 and $2.9 \times 10^{17} \text{ m}^{-3}$ in D_2 . Although n_e might be unreliable
 324 because of electron magnetization, this data completes the set of quantities which can
 325 be obtained only relying on the LP laser photodetachment technique.

326 The n_e profiles are obtained from the analysis of IV curves taken with the same LP
 327 used for laser photodetachment. The electron energy distribution function (EEDF) is
 328 calculated using the Druyvesteyn formula [30] and the second derivative of the measured
 329 electron current is calculated with a Savitzky-Golay filter to obtain the floating and
 330 plasma potential. An effective electron temperature T_e and the total electron density
 331 are then obtained by numerically integrating the EEDF. More details on the analysis

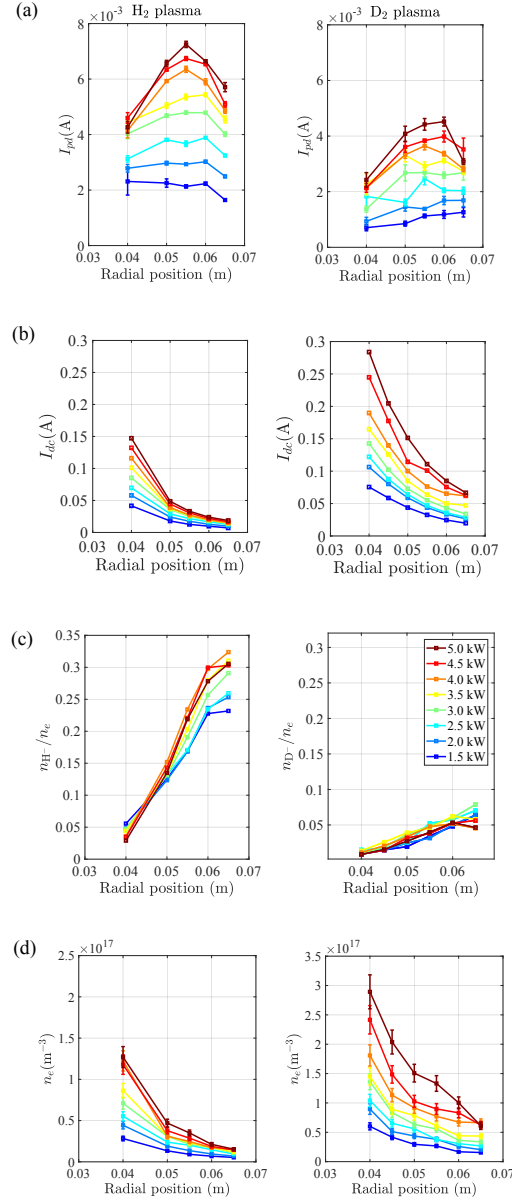


Figure 8. Results of the laser photodetachment measurements for H₂ (left column) and D₂ (right column) plasmas at 0.3 Pa: (a) Photodetachment amplitudes I_{pd} ; (b) Electron current I_{dc} collected when the probe is biased at $V_{bias} = 26$ V, above the plasma potential; (c) Ratio n_-/n_e ; and (d) Electron density n_e . On the edge of the plasma column, hydrogen plasma has lower electron density and a higher ratio n_-/n_e .

332 can be found in [31]. The higher density in D₂ is measured by microwave interferometry
 333 at the edge, at measurement position $r = 0.04$ m, revealing a line-integrated density a
 334 factor 2 higher in the case of deuterium.

335 The data shown in Fig. 8(a), (b) and (d) can be used to calculate the negative ion density,
 336 which is reported in Fig. 9. Negative ion density peaks at $r \sim 0.055$ m and H⁻ and D⁻
 337 are distributed in a shell-like shape, as also measured by OES [6]. The peak density of
 338 H⁻ is $7.7 \times 10^{15} \text{ m}^{-3}$ which is a factor ~ 2.5 lower compared to $2.0 \times 10^{16} \text{ m}^{-3}$ measured

339 via OES [6]. The disagreement between OES and laser photodetachment might be due
 340 to an imprecise estimate of n_e via LPs.

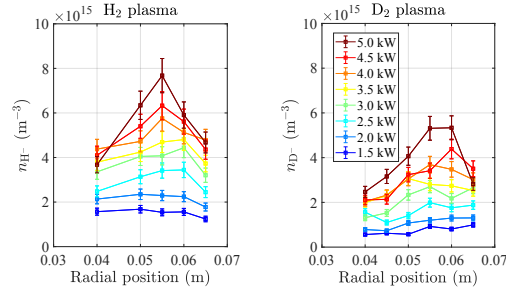


Figure 9. Radial profiles of negative ion density obtained with laser photodetachment and measuring the electron density via IV curves. These data are not calibrated with CRDS.

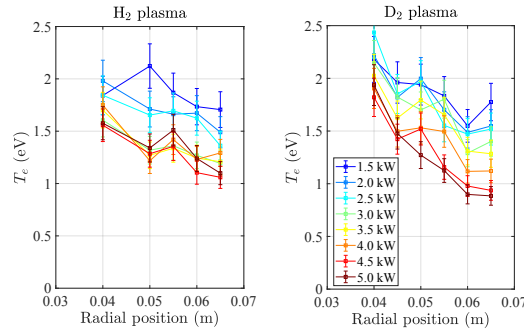


Figure 10. Electron temperature profiles showing the weak dependence with the RF power and the weak variation over the range of measurement. The low value of electron temperature in this range is favorable for the production of negative ions by dissociative attachment (DA).

341 For completeness we also show the temperature profiles in Fig. 10. T_e decreases
 342 weakly along the radial direction down to 1 eV at $r = 0.065$ m and 5 kW of power
 343 for both H₂ and D₂. Moreover, a general decrease of T_e is observed for increasing RF
 344 power. The T_e values in the edge are in the range where the DA cross section peaks,
 345 depending on the rovibrational state of H₂(v) and D₂(v). Thus, the T_e profiles show
 346 that the electron cooling on the edge, caused by the magnetic field needed to sustain
 347 the helicon discharge, is also effective to reach a favorable electron temperature for DA
 348 process.

349 4.3. CRDS combining with LP-assisted laser photodetachment to extract absolute 350 negative ion density profiles

351 In this section, we focus only on the data at 0.3 Pa, since this is the pressure relevant to
 352 present NBIs systems, such as the system designed for ITER, although lower pressure

353 may be more relevant for future systems [32]. The measurement of n_e via LPs in a plasma
 354 where electron are magnetized, might lead to error on the final estimate of negative ion
 355 density, n_- , when n_- is deduced from (6). To overcome this problem one can use the
 356 line-integrated negative ion density measured with CRDS for absolute calibration. The
 357 negative ion density profiles obtained with laser photodetachment shown in Fig. 9(a)
 358 and Fig. 9(b) might be not precise in absolute value but anyway proportional to n_- .
 359 Thus, they can be still used to extract the width and the position of the negative ion
 360 shell. Fig. 11(a) and (b) show the relative n_- profiles with the Gaussian fits, the position
 361 of CRDS line-of-sight and of the vessel wall.

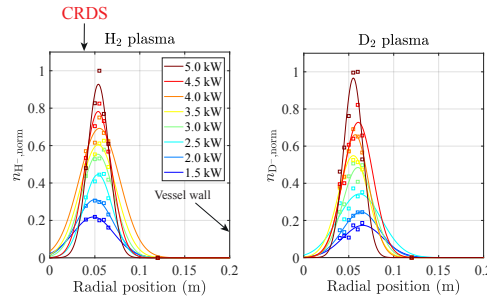


Figure 11. Gaussian fits of the relative n_- profiles measured with laser photodetachment. The position of CRDS line-of-sight to calibrate n_- absolute profiles and the vessel wall position is indicated.

362 The fit is performed with a Gaussian function, based on previous n_{H^-} profiles
 363 measured with OES [6]. The region at $r < 0.04$ m is not taken into account for
 364 the estimate of the absolute n_- profile since CRDS measures the density outside this
 365 measurement position. We define $F(x, y)$ as the normalized n_- profile at a certain RF
 366 power, where x and y are coordinates in the plane transverse to the plasma column axis,
 367 shown in Fig. 4(b). $F(x, y)$ is the function having the role of form factor, thus giving the
 368 shape of the negative ion density profile. The absolute negative ion density $n_-(x, y)$,
 369 shown in Fig. 4(b), can be written as:

$$370 \quad n_-(x, y) = n_-^{peak} F(x, y), \quad (7)$$

371 where n_-^{peak} is the negative ion peak density. CRDS measures the integral of (7)
 372 along the line of sight at the measurement position $y = y_{CRDS}$, which is:

$$373 \quad \bar{n}_-^{CRDS} = n_-^{peak} \int_{x_1}^{x_2} F(x, y_{CRDS}) dx, \quad (8)$$

374 where x_1 and x_2 are the integration limits along the line of sight. From (8) one can
 375 deduce n_-^{peak} which, inserted in (7), provides the absolute negative ion density profile.
 376 Fig. 12 shows the absolute n_{H^-} and n_{D^-} profiles only for 2, 3 and 5 kW RF powers for
 377 clarity. The peak value obtained at 5 kW for H_2 is $1.9(\pm 0.3) \times 10^{16} \text{ m}^{-3}$, close to the
 378 value measured by OES [6], which was $3.0(\pm 0.8) \times 10^{16} \text{ m}^{-3}$. For D^- the peak value

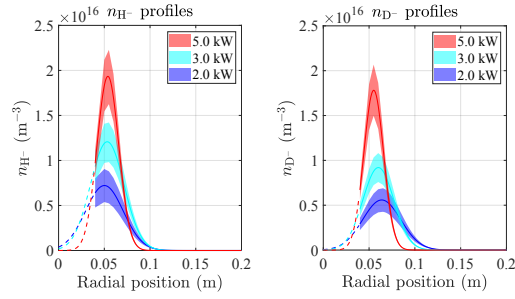


Figure 12. n_{H^-} and n_{D^-} radial profiles for different powers obtained using the relative negative ion profiles measured with laser photodetachment and calibrated with CRDS line-integrated measurements.

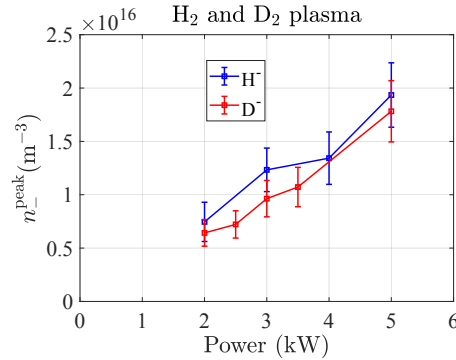


Figure 13. Peak negative ion density as a function of RF power at 0.3 Pa. n_- increases with power and higher density is observed in the case of H^- .

379 for 5 kW results in $1.8 (\pm 0.3) \times 10^{16} m^{-3}$, a bit low compared to $4.5 (\pm 2.0) \times 10^{16} m^{-3}$
 380 measured with OES.

381 In Fig. 13, we plot the peak value of n_- for increasing powers, showing a linear
 382 trend. The isotope effect seems to result in a slightly higher negative ion density for the
 383 case of hydrogen, but this is comparable to the error bar. Furthermore, in Fig. 14 we
 384 plot the negative ion density with electron density measured by the LP at $r = 0.055$ m,
 385 close to n_- peak values. n_- increases almost linearly with n_e and higher values may be
 386 attained by increasing the RF power. Even though the absolute value of n_e might be
 387 incorrect, the lower ratio n_-/n_e in the case of deuterium is clearly visible. This suggests
 388 that the co-extracted electrons might be a more important issue for D^- extraction.

389 The isotopic effect in negative ion and electron density has been investigated by
 390 some authors and it is due to a combination of different phenomena [33, 34, 35].
 391 Calculations and experiments show that n_e is higher in deuterium than hydrogen
 392 plasmas and is mostly due to ion transport. Positive ions are indeed mostly lost by
 393 transport to the walls where they are neutralized. For deuterium, the transport of
 394 positive ions is a factor $1/\sqrt{2}$ smaller than hydrogen because of the mass difference.
 395 This might explain in part the higher n_e in deuterium [33]. Concerning the isotope

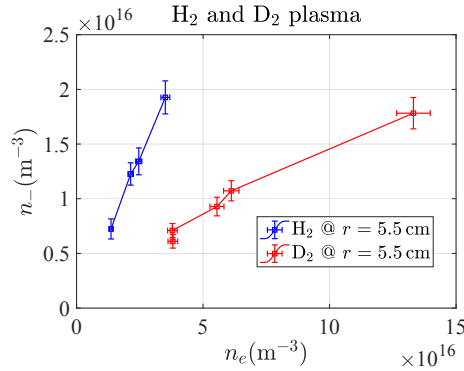


Figure 14. Negative ion density vs. electron density in hydrogen and deuterium plasmas.

396 effect on the negative ion density, the lower negative ion density in deuterium might be
 397 due to the higher degree of dissociation in deuterium leading to increased V-t cooling
 398 (cooling of $\text{D}_2(\text{v})$ in collision with D) and then less efficient D^- production [33]. For a
 399 better understanding of the processes, modeling is envisaged.

400 5. Discussion and Conclusions

401 The measurements performed with CRDS and LP-assisted photodetachment show that
 402 H^- and D^- are produced both in hydrogen and deuterium helicon plasmas in steady
 403 state regime with significant densities in volume production mode, without using
 404 caesium and with a few kW RF power. The measurements were performed at a
 405 fill pressure of 0.3 Pa, relevant to NBIs of ITER. Future NBIs may require lower fill
 406 pressures, and future studies at those pressures will be required [32]. We showed that LP-
 407 assisted photodetachment is not sufficient alone to obtain reliable measurements. Thus,
 408 to extract the absolute negative ion density profile, LP-assisted laser photodetachment is
 409 employed in combination with line-integrated measurements of CRDS. The LP-assisted
 410 laser photodetachment is used to measure the relative negative ion density profile
 411 showing that it is peaked off-axis. The line-integrated measurement performed by CRDS
 412 is then used to obtain the absolute negative ion density profile. Taking into account the
 413 peak negative ion density at 5 kW RF power, H^- density reaches $1.9 (\pm 0.3) \times 10^{16} \text{ m}^{-3}$,
 414 close to $3.0 (\pm 0.3) \times 10^{16} \text{ m}^{-3}$ measured with OES. However, D^- reaches $1.8 \times 10^{16} \text{ m}^{-3}$
 415 quite lower if compared to $4.5 (\pm 2.0) \times 10^{16} \text{ m}^{-3}$ measured with OES. The reason for
 416 this disagreement in the D_2 case is under investigation. Despite the absolute H^- and D^-
 417 densities appear to be comparable, the ratio n_-/n_e is about 6 times lower in deuterium
 418 than hydrogen. This suggests that the co-extracted electrons might be a more important
 419 issue for deuterium, if the current magnetic geometry is employed.

420 We believe that these experimental investigations add relevant data on the volume
 421 production of H^- and D^- in hydrogen and deuterium helicon plasmas. However, the
 422 design of a source based on a helicon plasma requires the investigation of different

423 magnetic field geometries and the compatibility with an extractor and an acceleration
424 system. Thus, a next step with the current system is the characterization of negative
425 ions along the plasma column and the study of different magnetic geometries, such as
426 the expanding magnetic field, with the diagnostics mentioned in this paper. In parallel
427 with this, 3D numerical simulations could be an important tool to predict the negative
428 ion production as a function of source parameters.

429 If used as part of a future ion source for an NBI system, direct extraction of the
430 negative ions from the plasma column in the radial or axial direction should be possible.
431 If radial extraction is used, because of the inherent cylindrical nature of the helicon
432 driven plasma, the beam would have to be long and narrow, such as that suggested
433 in reference [36]. However significant development may be needed if the extractor
434 perturbs significantly the plasma and because the extraction system would need to
435 be segmented, with each segment fitting between the magnetic coils. Axial extraction
436 seems unattractive as the annular region from which ions could be extracted is short, and
437 hence the extracted current would be low, and a transverse filter field would probably
438 be needed to reduce the co-extracted electron current. It is also to be noted that the
439 resulting annular beam shape has no particular advantage from the point of view of
440 neutralisation or beamline design.

441 Using the helicon device to provide a plasma that expands towards a conventional
442 multi-aperture system with a caesiated plasma grid should be considered because of
443 the ease of operation at fill pressures < 0.3 Pa and the high efficiency of the helicon
444 device. In this case, it needs to be established that the helicon driven plasma produces
445 sufficient dissociation of the gas in order to have sufficient negative ion production via
446 the impingement of the atoms on the low work function of the plasma grid surface.

447 **Acknowledgments**

448 This work has been carried out within the framework of the EUROfusion Consortium
449 and has received funding from the Euratom research and training programme 2014
450 - 2018 and 2019 - 2020 under grant agreement No 633053. The views and opinions
451 expressed herein do not necessarily reflect those of the European Commission. This
452 work was supported in part by the Swiss National Science Foundation. We gratefully
453 acknowledge the mechanical and electronic workshops of the Swiss Plasma Center for
454 their collaboration.

455 **Bibliography**

- 456 [1] G. Serianni, P. Agostinetti, M. Agostini, D. Aprile, C. Baltador, M. Barbisan, M. Brombin, M.
457 Cavenago, G. Chitarin, M. Dalla Palma, R. Delogu, F. Fellin, N. Fonnesu, N. Marconato, R.
458 Pasqualotto, A. Pimazzoni, E. Sartori, S. Spagnolo, M. Spolaore, P. Veltri, B. Zaniol and M.
459 Zaupa, *New J. Phys.* **19**, 045003 (2017).

- 460 [2] R. S. Hemsworth, D. Boilson, P. Blatchford, M. Dalla Palma, G. Chitarin, H.P.L. de Esch, F. Geli,
461 M. Dremel, J. Graceffa, D. Marcuzzi, G. Serianni, D. Shah, M. Singh, M. Urbani and P. Zaccaria,
462 New J. Phys. **19**, 025005 (2017).
- 463 [3] U. Fantz, C. Hopf, D. Wunderlich, R. Friedl, M. Fröschle, B. Heinemann, W. Kraus, U. Kurutz, R.
464 Nocentini and L. Schiesko, Nucl. Fusion **57**, 116007 (2017).
- 465 [4] P. Sonato, P. Agostinetti, U. Fantz, I. Furno, A. Simonin and M. Q. Tran, New J. Phys. **18**, 125002
466 (2016).
- 467 [5] S. Briefi and U. Fantz, AIP Conf. Proc., **1515**, 278 (2013).
- 468 [6] C. Marini, R. Agnello, B. P. Duval, I. Furno, A. A. Howling, R. Jacquier, A. N. Karpushov, G.
469 Plyushchev, K. Verhaegh, and Ph. Guittienne, Nucl. Fusion **57**, 036024 (2017).
- 470 [7] S. Shinoara, Advances in Physics: X, 3:1, **3**(1):1420424, (2018).
- 471 [8] I. Furno, R. Agnello, U. Fantz, A. Howling, R. Jacquier, C. Marini, G. Plyushchev, Ph. Guittienne,
472 and A. Simonin, EPJ Web Conf. **157**, 03014 (2017).
- 473 [9] J. Santoso, R. Manoharan, S. O'Byrne and C. S. Corr, Phys. Plasmas **22**, 093513 (2015).
- 474 [10] A. Pandey, D. Mukherjee, D. Borah, M. Bandyopadhyay, H. Tyagi, R. Yadav and A. Chakraborty
475 Plasma Phys. Control. Fusion **61**, 065003 (2019).
- 476 [11] P. Guittienne, E. Chevalier and Ch. Hollenstein, J. Appl. Phys. **98**, 083304 (2005).
- 477 [12] I. Furno, R. Agnello, A. A. Howling, R. Jacquier, G. Plyushchev, Ph. Guittienne, M. Barbisan, R.
478 Pasqualotto, S. Béchu, I. Morgal and A. Simonin, 60th Annual Meeting of the APS Division of
479 Plasma Physics, Portland, Oregon (USA).
- 480 [13] R. Jacquier, R. Agnello, B. Duitel, C. Marini, Ph. Guittienne, A. A. Howling, I. Furno, G.
481 Plyushchev, A. Simonin, I. Morgal and S. Béchu, Fusion Eng. Des. **146**, 1140-1144 (2019).
- 482 [14] R. Agnello, M. Barbisan, I. Furno, Ph. Guittienne, A. Howling, R. Jacquier, R. Pasqualotto, G.
483 Plyushchev, Y. Andrebe, S. Béchu, I. Morgal and A. Simonin, Rev. Sci. Instrum. **89**, 103504
484 (2018).
- 485 [15] M. Berger, U. Fantz, S. Christ-Koch and NNBI Team, Plasma Sources Sci. Tech. **18**, 025004
486 (2009).
- 487 [16] M. A. Lieberman and A. J. Lichtenberg, *Principles of plasma discharges and materials processing*
488 (John Wiley and Sons, New York, 1994).
- 489 [17] I. D. Sudit and F. F. Chen, Plasma Sources Sci. Technol. **5**, 43 (1996).
- 490 [18] J. N. Bardsley, J. Phys. B: At. Mol. Phys. **1**, 349 (1968).
- 491 [19] J. S. Schultz, Rev. Mod. Phys. **45**, 423 (1973).
- 492 [20] M. Bacal, Nucl. Fusion **46**, S250-S259 (2006).
- 493 [21] J. R. Hiskes, J. Appl. Phys. **51**, 4592 (1980).
- 494 [22] A. O'Keefe and D. G. Deacon, Rev. Sci. Instrum. **59**, 2455 (1988).
- 495 [23] H. Nakano, K. Tsumori, M. Shibuya, S. Geng, M. Kasaki, K. Ikeda, K. Nagaoka, M. Osakabe, Y.
496 Takeiri and O.Kaneko, in 17th International Symposium on Laser-Aided Plasma Diagnostics,
497 (IOP Publishing, 2015), p.3.
- 498 [24] R. Pasqualotto, A. Alfier and L. Lotto, Rev. Sci. Instrum. **81**, 10D710 (2010).
- 499 [25] M. Bacal, Rev. Sci. Instrum. **71**, 3981 (2000).
- 500 [26] P. Devynck, J. Auvray, M. Bacal, P. Berlemont, J. Bruneteau, R. Leroy, and R. A. Stern, Rev.
501 Sci. Instrum. **60**, 2873 (1989).
- 502 [27] S. Aleiferis, *Experimental Study of H⁻ negative ion production by electron cyclotron resonance*
503 *plasmas*, Université Grenoble-Alpes, PhD thesis (2016).
- 504 [28] L. Friedland, C. I. Ciubotariu, and M. Bacal, Phys. Rev. E **49**, 4353 (1994).
- 505 [29] S. Christ-Koch, U. Fantz, M. Berger and NNBI Team, Plasma Sources Sci. Tech. **18**, 025003
506 (2009).
- 507 [30] M. J. Druyvesteyn, Z. Phys. **64**, 781 (1930).
- 508 [31] S. Béchu, A. Soum-Glaude, A. Bs, A. Lacoste, P. Svarnas, S. Aleiferis, A. A. Ivanov and M. Bacal
509 Phys. Plasmas **20**, 101601 (2013).
- 510 [32] R. S. Hemsworth and D. Boilson, AIP Conference Proceedings **1869**, 060001 (2017).

- 511 [33] D. A. Skinner, A. M. Bruneteau, P. Berlemont, C. Courteille, R. Leroy, and M. Bacal, Phys. Rev.
512 E **48**, 2122 (1993).
- 513 [34] A. M. Bruneteau, C. Courteille, R. Leroy, and M. Bacal, Rev. Sci. Instrum. **67**, 3827 (1996).
- 514 [35] O. Fukumasa and K. Yoshino, Rev. Sci. Instrum. **69**, 941 (1998).
- 515 [36] A. Simonin, R. Agnello, S. Béchu, J. M. Bernard, C. Blondel, J. P. Boeuf, D. Bresteau, G. Cartry,
516 W. Chaibi, C. Drag, B. P. Duval, H. P. L. de Esch, G. Fubiani, I. Furno, C. Grand, Ph. Guittienne,
517 A. Howling, R. Jacquier, C. Marini and I. Morgal, New J. Phys. **18**, 125005 (2016).